

PAPER • OPEN ACCESS

Finite diffusion microsegregation model applied to multicomponent alloys

To cite this article: V. Maguin *et al* 2019 *IOP Conf. Ser.: Mater. Sci. Eng.* **529** 012029

View the [article online](#) for updates and enhancements.



IOP | ebooks™

Bringing you innovative digital publishing with leading voices to create your essential collection of books in STEM research.

Start exploring the **collection** - download the first chapter of every title for free.

Finite diffusion microsegregation model applied to multicomponent alloys

V. Maguin^{1,2}, G. Guillemot¹, V. Jaquet², N. T. Niane², L. Rougier², D. Daloz³, J. Zollinger³ and Ch.-A. Gandin¹

¹ MINES ParisTech, PSL Research University, CEMEF – Centre de mise en forme des matériaux, CNRS UMR 7635, CS 10207, 1 rue Clause Daunesse, F-06904 Sophia Antipolis Cedex, France

² Safran, site de Paris-Gennevilliers, 171 Boulevard de Valmy, F-92700 Colombes, France

³ Université de Lorraine, Institut Jean Lamour, CNRS UMR 7195, F-54011 Nancy, France

E-mail: vincent.maguin@mines-paristech.fr, vincent.maguin@safrangroup.com

Abstract. During casting, diffusion phenomena are often simplified by Lever-Rule or Gulliver-Scheil hypotheses, thus simplifying chemical diffusion to extreme configurations. The present work proposes an extension of the Tong-Beckermann microsegregation model to multicomponent alloys while considering finite diffusion in liquid and solid phases plus the effect of tip undercooling of the columnar front. The behaviour of this model is studied according to the solidification conditions (growth velocity and thermal gradient) and comparison with microprobe measurements is proposed for a seven components nickel-base superalloy.

1. Introduction

Upon solidification of metallic alloys, complex segregation and diffusion phenomena occur during the growth of the dendritic microstructure. Several microsegregation models can be used to determine the solidification path. The Lever-Rule (LR) solidification path assumes full equilibrium in the liquid and solid phases, equivalent to complete diffusion of all chemical species. The solid fraction is evaluated according to the tie line for the nominal composition. However, diffusion in solid and liquid phases differs by several orders of magnitude. Typical cooling rates during casting do not allow reaching the thermodynamic equilibrium. The Gulliver-Scheil (GS) solidification path only considers thermodynamic equilibrium between a small portion of solid at the interface with liquid phase, thus incrementally accumulating solid with various compositions as no solid diffusion. Both Lever-Rule and Gulliver-Scheil models are approximations mainly because they do not consider the microstructure undercooling and finite diffusion in all phases. Brody and Flemings [1] and Clyne and Kurz [2] proposed models accounting for finite (and non-zero) diffusion in the solid phase. Wang and Beckerman [3] simplified the dendritic network to three domains (1) solid, (2) interdendritic liquid and (3) extradendritic liquid. Tong and Beckerman (TB) [4] proposed a modification where the Fourier number in the liquid can be estimated thanks to a function of the dendrite tip supersaturation. Their model was applied to columnar solidification without diffusion in the solid phase for a binary Ag - 15 wt.% Cu alloy. Linearisation of the phase diagram was assumed.

In the present work, the equations of the TB model are written for whatever multicomponent



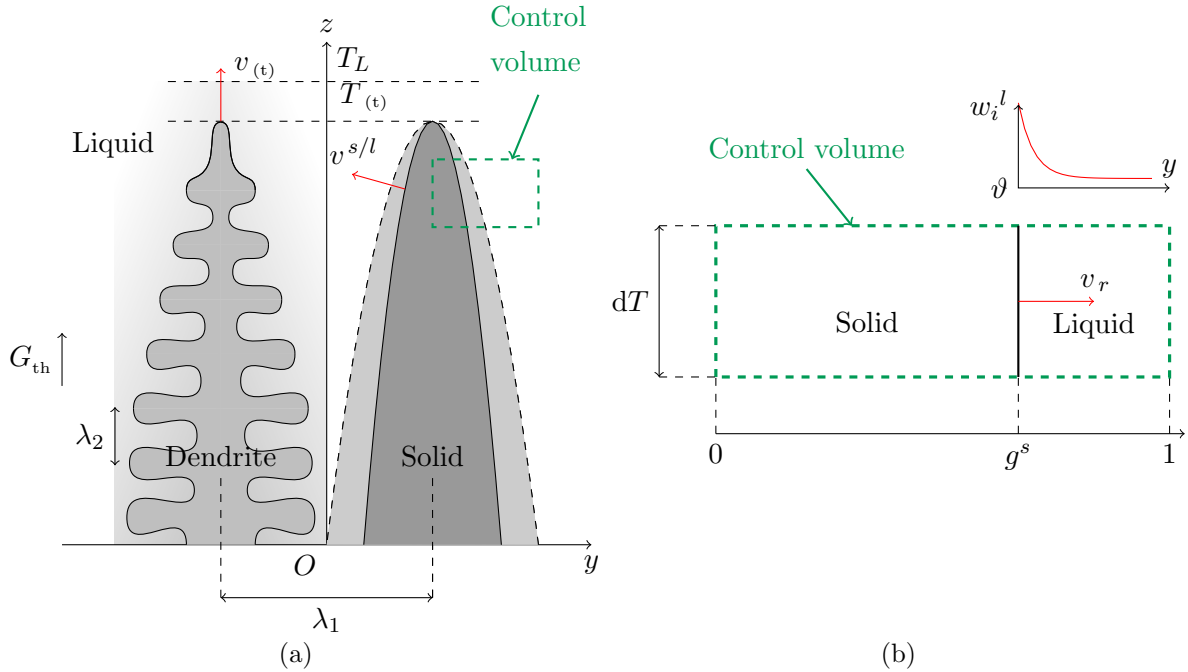


Figure 1: Schematics of (a, left) a columnar dendrite and (a, right) its simplification with (b) the control volume for mass balances. (Inspired from [4])

alloy including diffusion in solid phase. This microsegregation model is directly coupled with a dendrite tip model which considers the solidification conditions.

2. General equations

The present model describes the growth of a columnar dendritic network in the same direction as the temperature gradient, G_{th} , with a primary arm spacing, λ_1 , as schematized in fig. 1a. The dendrite tips grow with velocity $v_{(t)}$ at temperature $T_{(t)}$. The complex shape of the primary trunk (fig. 1a, left) is simplified by a dendrite envelope (fig. 1a, right). The equations are written for a control volume (fig. 1b) defined by the green rectangle in fig. 1a, *i.e.* in which solidification proceeds directionally over a distance $\lambda_1/2$ at a temperature evolving with time according to $T = T_{(t)} + G_{th} \cdot v_{(t)} \cdot t$. Velocity $v^{s/l}$ is then approximated by a radial contribution v_r .

2.1. Dimensionless quantities

This model is written with a dimensionless form. Chemical diffusion is described by Fourier numbers for each chemical specie i according the ratios:

$$F_i^l = \frac{D_i^l t_s}{(\lambda_1/2)^2} \quad (1a) \quad F_i^s = \frac{D_i^s t_s}{(\lambda_2/2)^2} \quad (1b)$$

where D_i^l and D_i^s are the chemical diffusion coefficients for the liquid and solid phases, respectively. The model associates the Fourier number in the liquid phase with the primary dendrite arm spacing, λ_1 , and the Fourier number in the solid phase with the secondary dendrite arm, λ_2 . These two different characteristic lengths were already used by Wang and Beckermann [3] for a dendritic microstructure. The solidification time, t_s , is firstly estimated according a Lever-Rule solidification interval ΔT_0 (taking into account the possible eutectic temperature)

and the cooling rate \dot{T} , $t_s = \Delta T_0 / \dot{T}$. However another Fourier number \widetilde{F}_i^l is defined for the liquid phase as:

$$\widetilde{F}_i^l = \tilde{\sigma}_i F_i^l = \tilde{\sigma}_i \frac{D_i^l t_s}{(\lambda_1/2)^2}. \quad (1c)$$

The estimation of this modified Fourier number is determined later according to the working point of the dendrite tip. The constant $\tilde{\sigma}_i$ is evaluated for each chemical specie for a given value of the primary dendrite arm spacing.

For the dendrite tip the chemical Péclet number, Pe_{c_i} , is defined for each solute i as:

$$Pe_{c_i} = \frac{r_{(t)} v_{(t)}}{2 D_i^l}, \quad (2)$$

with $r_{(t)}$ and $v_{(t)}$ the radius and the growth velocity of the dendrite tip, respectively. It is worth noticing that a stationary growth regime is assumed so $v_{(t)} = v_L$, where v_L is the velocity of the liquidus isotherm T_L .

2.2. Solute balances

Three mass balances for each solute i describe the system for liquid and solid phases and for the control volume [4]. In the liquid phase, figure 1b gives a schematic representation of the concentration profile in the lateral growth direction $O\vec{y}$ by assuming no diffusion of solute in the main solidification direction $O\vec{z}$. This profile is expressed as :

$$\frac{w_i^l - w_{i0}}{w_i^{l(s/l)} - w_{i0}} = \exp \left(-\frac{1}{\widetilde{F}_i^l g^s} \frac{y}{\lambda_1} \right), \quad (3)$$

where w_i^l represents the liquid composition for a y position in the liquid phase, w_{i0} is the nominal composition of the alloy and $w_i^{l(s/l)}$ is the composition of liquid at the solid/liquid interface. By integration of eq. (3) in the liquid phase, the mean composition $\langle w_i \rangle^l$ for each solute i takes the form:

$$\frac{\langle w_i \rangle^l - w_{i0}}{w_i^{l(s/l)} - w_{i0}} = \frac{2\widetilde{F}_i^l g^s}{(1 - g^s)} [1 - \mathcal{F}_i(g^s)] \quad (4)$$

with for each solute: $\mathcal{F}_i(g^s) = \exp \left(-(1 - g^s) / (2\widetilde{F}_i^l g^s) \right)$.

For the solid phase the solute mass balance in the solid phase for each solute i is written [3]:

$$g^s \frac{d\langle w_i \rangle^s}{dg^s} = (1 + 6F_i^s) \left(w_i^{s(s/l)} - \langle w_i \rangle^s \right). \quad (5)$$

The last solute balance for each solute i is expressed for the whole control volume:

$$g^s \langle w_i \rangle^s + g^l \langle w_i \rangle^l = w_{i0} \quad \text{with} \quad g^s + g^l = 1, \quad (6)$$

2.3. Phase diagram for multicomponent alloy

The present microsegregation model is coupled with a phase diagram. For a working point $(T, w_i^{l(s/l)})$ the liquidus surface follows the relationship:

$$T = T_{L0} + \sum_i m_{Li} \left(w_i^{l(s/l)} - w_{i0} \right) \quad (7)$$

with T_{L0} is the liquidus temperature for a given reference composition w_{i0} . The solid interfacial composition $w_i^{s(s/l)}$ is defined by the tie line relation according to the segregation coefficient k_i :

$$k_i = \frac{w_i^{s(s/l)}}{w_i^{l(s/l)}}, \quad (8)$$

3. Numerical Solution

3.1. General solution

This section presents the solution methods in order to solve the equations of this microsegregation model. With combination of equations (4), (5) and (6), a single equation is obtained for each solute i :

$$\mathcal{G}_{1_i}(g^s) \frac{dw_i^{l(s/l)}}{dg^s} = \mathcal{G}_{2_i}(g^s, w_i^{l(s/l)}, w_i^{s(s/l)}), \quad (9)$$

with

$$\begin{cases} \mathcal{G}_{1_i}(g^s) &= \widetilde{2F}_i^l g^s (1 - \mathcal{F}_i(g^s)) \\ \mathcal{G}_{2_i}(g^s, w_i^{l(s/l)}, w_i^{s(s/l)}) &= (1 + 6F_i^s) (w_{i0} - w_i^{s(s/l)}) \\ &+ (w_i^{l(s/l)} - w_{i0}) \left(\frac{\mathcal{F}_i(g^s)}{g^s} - 2\widetilde{F}_i^l (1 + 6F_i^s) (1 - \mathcal{F}_i(g^s)) \right) \end{cases} \quad (10)$$

By the Newton integration method of this 1st order differential equation, the increments of the interfacial compositions in liquid phase $w_i^{l(s/l)}$ are estimated for a unique solid fraction step. The new interfacial composition in the solid $w_i^{s(s/l)}$ is deduced from the tie line equation (7). The temperature is evaluated *a posteriori* using the phase diagram and relation (7).

3.2. Initialisations

The modified Fourier number, \widetilde{F}_i^l , has to be evaluated in the microsegregation model. This is done by considering that Equation 9 must be consistent with the operating point of the dendrite tip. In this way the differential equation is evaluated for $g^s = 0$, at the beginning of the solidification. By remarking that \mathcal{G}_{1_i} -functions reaches the zero-value and by solving the systems $\lim_{g^s \rightarrow 0} \mathcal{G}_{2_i}(g^s, w_i^{l(s/l)}, w_i^{s(s/l)}) = 0$, one can show that:

$$\widetilde{F}_i^l = \frac{w_{i0} - w_{i(t)}^{s(s/l)}}{2(w_{i(t)}^{l(s/l)} - w_{i0})} \quad \text{or} \quad \tilde{\sigma}_i = \frac{1 - \text{Iv}(\text{Iv}(Pe_i))}{2 \text{Iv}(Pe_i)}, \quad (11)$$

where $w_{i(t)}^{s(s/l)}$ and $w_{i(t)}^{l(s/l)}$ represent respectively the interfacial composition at the tip in solid and liquid phases. The working point of the dendrite tip and also $(w_{i(t)}^{s(s/l)}, w_{i(t)}^{l(s/l)})$ quantities are estimated with a KGT dendrite tip model [5] applied to multicomponent alloys [6]:

$$w_{i(t)}^{l(s/l)} = \frac{w_{i0}}{1 - (1 - k_i) \text{Iv}(Pe_{c_i})}, \quad (12)$$

where $\text{Iv}(x)$ represents the Ivantsov function of quantity x .

The tip radius computed using the KGT model is also used for evaluating the first interdendritic dendrite arm spacing according to Kurz's expression [7]:

$$\lambda_1 = \sqrt{\frac{3\Delta T_0 r_{(t)}}{G_{th}}} \quad (13)$$

| Ni | Cr | Co | Mo | W | Al | Ti | Ta |
|------|-----|-----|-----|-----|-----|-----|-----|
| Base | 7.8 | 6.5 | 2.0 | 5.7 | 5.2 | 1.1 | 7.9 |

Table 1: Nominal composition of AM1 [12]

| Case | G_{th} ($K \cdot cm^{-1}$) | v_L ($mm \cdot min^{-1}$) | Γ ($K \cdot m$) | $\propto D_i^s$ | λ_1 (μm) | λ_2 (μm) |
|------|--------------------------------|-------------------------------|--------------------------|-----------------|-------------------------|-------------------------|
| #T1 | 40 | 6 | 10^{-11} | $\times 1$ | 196 | 196 |
| #T2 | 40 | 6 | 10^{-11} | $\times 10^3$ | 196 | 196 |
| #E1 | 40 | 6 | 10^{-7} | $\times 1$ | 196 | 100 |
| #T3 | 1 | 6 | 10^{-7} | $\times 1$ | 1240 | 100 |
| #T4 | 40 | 100 | 10^{-7} | $\times 1$ | 97 | 100 |

Table 2: Cooling configurations for AM1 solidification paths

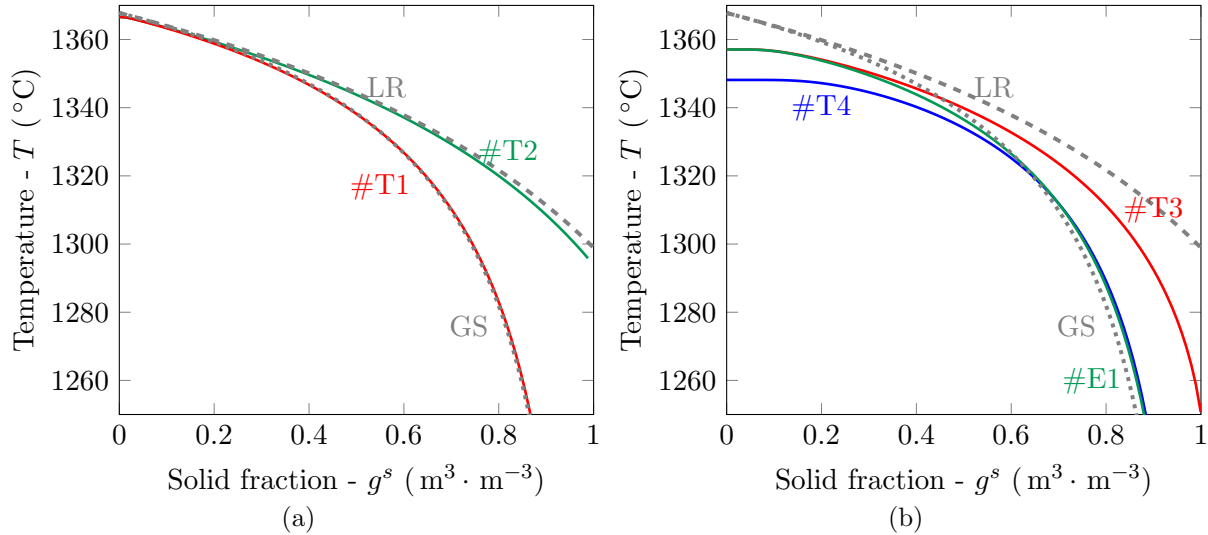


Figure 2: Solidification path for the AM1 superalloy, (a) validation of the model for cases (—) #T1 and (—) #T2 (b) effect of thermal gradient and growth velocity for cases (—) #E1, (—) #T3 and (—) #T4. For both graphs grey lines represent (---) Lever-Rule and (.....) Gulliver-Scheil.

4. Results and discussion

Firstly, a multicomponent nickel based superalloy (AM1), with nominal composition reported in Table 1, is considered. The model is validated for Lever-Rule and Gulliver-Scheil solidification paths. Then the effects of solidification conditions (growth velocity and thermal gradient) are studied. One comparison with experimental data is proposed. All thermodynamic and mobility properties are extracted from the NI25 [8] and MOBNI4 [9] databases. The linearization of the phase diagram and diffusion coefficients for each chemical species were computed with the Thermo-Calc interface.

4.1. Model's behaviour

AM1 is a 1st generation nickel based superalloy, daily used for the production of single crystal turbine blades of jet engines. Several solidification conditions are presented in table 2 in addition

| Case | G_{th} ($\text{K} \cdot \text{cm}^{-1}$) | v ($\text{mm} \cdot \text{min}^{-1}$) | λ_1 (μm) | λ_2 (μm) |
|------|---|---|-------------------------------|-------------------------------|
| #E1 | 40 | 6 | 196 | 100 |
| #E2 | 40 | 3 | 233 | 100 |
| #E3 | 40 | 0.5 | 364 | 110 |

Table 3: Cooling configurations for AM1 solidification experiments

with the primary and secondary dendrite arm spacing.

For the test cases #T1 and #T2, the Gibbs-Thomson coefficient Γ is fixed to an artificially small value, equal to $10^{-11} \text{ K} \cdot \text{m}$. In this way the tip undercooling is close to zero (fig. 2a). Due to the relative large arm spacing, the Fourier number is very small and thus diffusion in solid phase is limited. The case #T1 is close to the Gulliver-Scheil solidification path. For case #T2, the diffusion coefficients in solid phase are increased by 3 orders of magnitude, leading to a result that approaches the Lever-Rule approximation.

For cases #E1, #T3 and #T4 the Gibbs-Thomson coefficient is fixed to a consistent value of $10^{-7} \text{ K} \cdot \text{m}$. The secondary arm spacing is now set to a value of $100 \mu\text{m}$. Case #E1 is computed with a solidification condition of $G_{\text{th}} = 40 \text{ K} \cdot \text{cm}^{-1}$ and $v_L = 6 \text{ mm} \cdot \text{min}^{-1}$. The tip undercooling reaches a value of 10.7 K . When the temperature gradient is decreased to a value of $G_{\text{th}} = 1 \text{ K} \cdot \text{cm}^{-1}$ (case #T3), the modification on the working point of the tip remains limited. Due the increase of the solidification time the effect of the diffusion in solid is more pronounced. For $g^s > 0.4$ the solidification path comes closer to LR. For case #T4 the growth velocity is increased to $100 \text{ mm} \cdot \text{min}^{-1}$. The tip undercooling reaches 19.6 K . For $g^s > 0.6$ this solidification path is superposed to the case #E1 and close to GS.

4.2. Comparison with experimental results

Case #E1 corresponds to the solidification conditions examined by Zollinger and Daloz's experiments [10, 11]. The experimental points were obtained by micro-probe analyses in four cuts at 1350 , 1325 , 1300 and 1275°C of a directionally solidified cylindrical sample quenched during processing. Two other solidification conditions, #E2 and #E3 were investigated as presented in table 3. The evolutions of the solid fraction are compared to experimental points as well as the GS and LR solidification paths in fig. 3 while using $\Gamma = 10^{-7} \text{ K} \cdot \text{m}$.

Simulations are very different from experimental measurements. These differences can be firstly explained by the model assumptions. The model uses a linearization of the phase diagram at the liquidus temperature. One can evaluate its effect by considering the black line in fig. 3 providing the LR solidification path with full coupling with the CALPHAD database [8]. The corresponding Gulliver-Scheil path shows almost no difference with its counterpart using linearization and thus is not plotted. Direct coupling of the present microsegregation model with thermodynamic equilibrium may improve the results. Because the time cost for CALPHAD equilibrium is heavy, a direct CALPHAD-coupling is not compatible for coupling at macroscopic scale. The thermodynamic computation might be externalized and the tie lines gathered in tabulations [13]. For information purposes, the solidification path computation with the linearization hypothesis for the AM1 alloy needs only few seconds for a solid fraction integration step of 10^{-4} . It makes quite possible to use the present microsegregation model for coupling at macroscopic scale. The phase diagram storage has yet to balance the accuracy and the computation time. The tabulations also prevent convergence difficulties which are encountered for heavy thermodynamic databases during CALPHAD computations.

This model describes a columnar front growth for a constant nominal concentration. Due to relative low cooling rate (from $0.4 \text{ K} \cdot \text{s}^{-1}$ for case #E1 to $0.03 \text{ K} \cdot \text{s}^{-1}$ for case #E3), solute

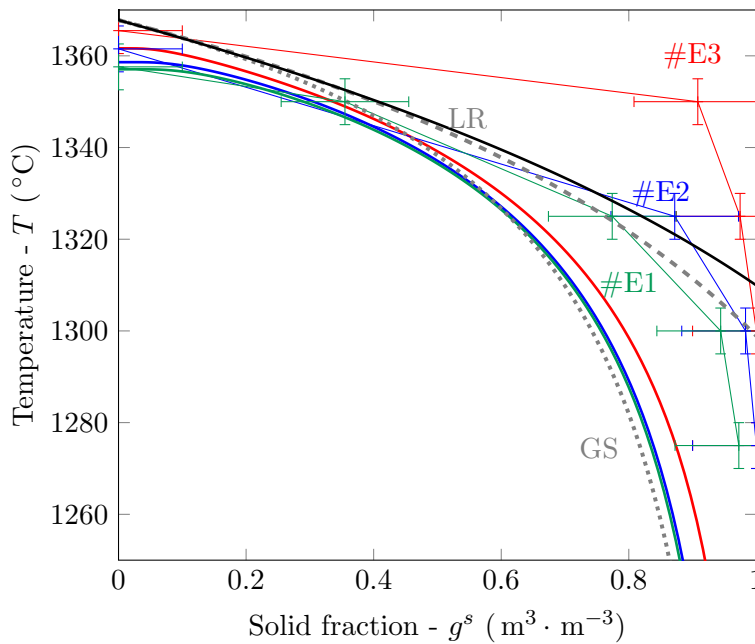


Figure 3: Comparison of solidification paths for the AM1 superalloy between (continuous lines, —) the microsegregation model and (—+) experimental data. The color is associated to case presented in table 2 (—) #E1, (—) #E2 and (—) #E3 configurations. Grey lines represent (---) Lever-Rule and (.....) Gulliver-Scheil. The black line (—) represents Lever-Rule with full CALPHAD coupling.

segregation phenomena through liquid flow is conceivable. This kind of effect cannot be described by a microsegregation model alone. A macrosegregation framework including solute transport and liquid flow is required. Diffusion coefficient are computed for the nominal composition at liquidus temperature and constant in the present model.

A constant λ_2 value for the entire solidification interval. However, λ_2 has been described by Zollinger and Daloz as a function $\propto t_s^{1/3}$. In this model diffusion in the solid is underestimated at the beginning of the solidification path. In addition, measurement report that λ_2 measurement is independent of cooling rate even though the ratio between the lowest and highest cooling rates is 12. Due to coarsening, the measurement of the secondary arm spacing also is over-evaluated by the *post mortem* analysis. A time-dependant secondary arm spacing could increase the effect of diffusion in the solid phase. More broadly, the confidence of the thermodynamic and diffusion database could also be discussed.

5. Conclusions

The present work is an extension of the Tong-Beckermann's microsegregation model for a multicomponent alloy with consideration of diffusion in solid and liquid phases. Solidification paths similar to LR and GS were obtained by artificially changing the Gibbs-Thomson and diffusion coefficients. The comparison with experimental data gives good prediction of the tip undercooling and coherent evolutions when changing the processing parameters. In order to improve this model, direct coupling with tabulated thermodynamic equilibrium is being conducted.

References

- [1] H. D. Brody and M. C. Flemings 1966 *Trans. TMS-AIME* 236 615

- [2] T. W. Clyne and W. Kurz 1981 *Metallurgical Transactions A* **12** **6** 965-71
- [3] C.Y. Wang and C. Beckermann 1993 *Materials Science and Engineering A* **171** 199-211
- [4] X. Tong and C. Beckermann 1998 *Journal of crystal growth* **2** **187** 289-302
- [5] W. Kurz, B. Giovanola and R. Trivedi 1986 *Acta metallurgica* **34** **5** 823-30
- [6] W. J. Boettinger 2016 *Journal of phase equilibria and diffusion* **37** **1** 4-18
- [7] W. Kurz and D. J. Fisher 1998 *Fundamentals of Solidification, Fourth Revised Edition* ed Trans Tech Publications p255-6
- [8] NI25 : Ni-based alloys and superalloy solutions database Thermo-Calc Software AB, 2017
- [9] MOBNI4 - TCS Nickel Mobility Database [Version 4.0 : May 2015] 2015
- [10] H. Ben Hamouda 2012 *Ecole Nationale Supérieure des Mines de Paris* <https://pastel.archives-ouvertes.fr/tel-01202342>
- [11] J. Zollinger and D. Daloz, 2010 Essais de trempe en cours de solidification sur AM1 : réalisation, expertises métallurgiques, synthèse
- [12] P. Caron and T. Khan 1999 *Aerospace Science and Technology* **3** **8** 513-523
- [13] A. Saad, Ch.-A. Gandin and M. Bellet 2015 *Comp. Mat. Sc.* **99** 221-31